PNAS
www.pnas.org

Supplementary Information for

Intrinsically stretchable electrode array enabled in vivo electrophysiological mapping of atrial fibrillation at cellular resolution

Jia Liu, Xinyuan Zhang, Yuxin Liu, Miguel Rodrigo, Patrick D. Loftus, Joy Aparicio-Valenzuela, Jukuan Zheng, Terrence Pong, Kevin J. Cyr, Meghedi Babakhanian, Jasmine Hasi, Jinxing Li, Yuanwen Jiang, Christopher J. Kenney, Paul J. Wang, Anson M. Lee, Zhenan Bao

Correspondence: Zhenan Bao and Anson M. Lee
Email: zbao@stanford.edu and ansonlee@stanford.edu

This PDF file includes:

Supporting Figures and Legends for Figures S1 to S8
Supporting Movie Legend for Movie S1

Other supplementary materials for this manuscript include the following:

Movie S1

www.pnas.org/cgi/doi/10.1073/pnas.2000207117

Supporting Figures and Legends

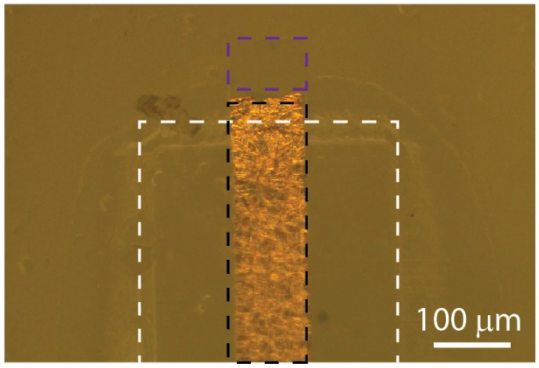

Fig. S1. Optical images of a representative elastic electrodes (elastrode). Bright field optical images of a representative single electrode from the elastrode array. The white, black and purple dashed boxes highlight regions for passivation layer, PEDOT:PSS/Au interconnections and PEDOT:PSS electrode regions.

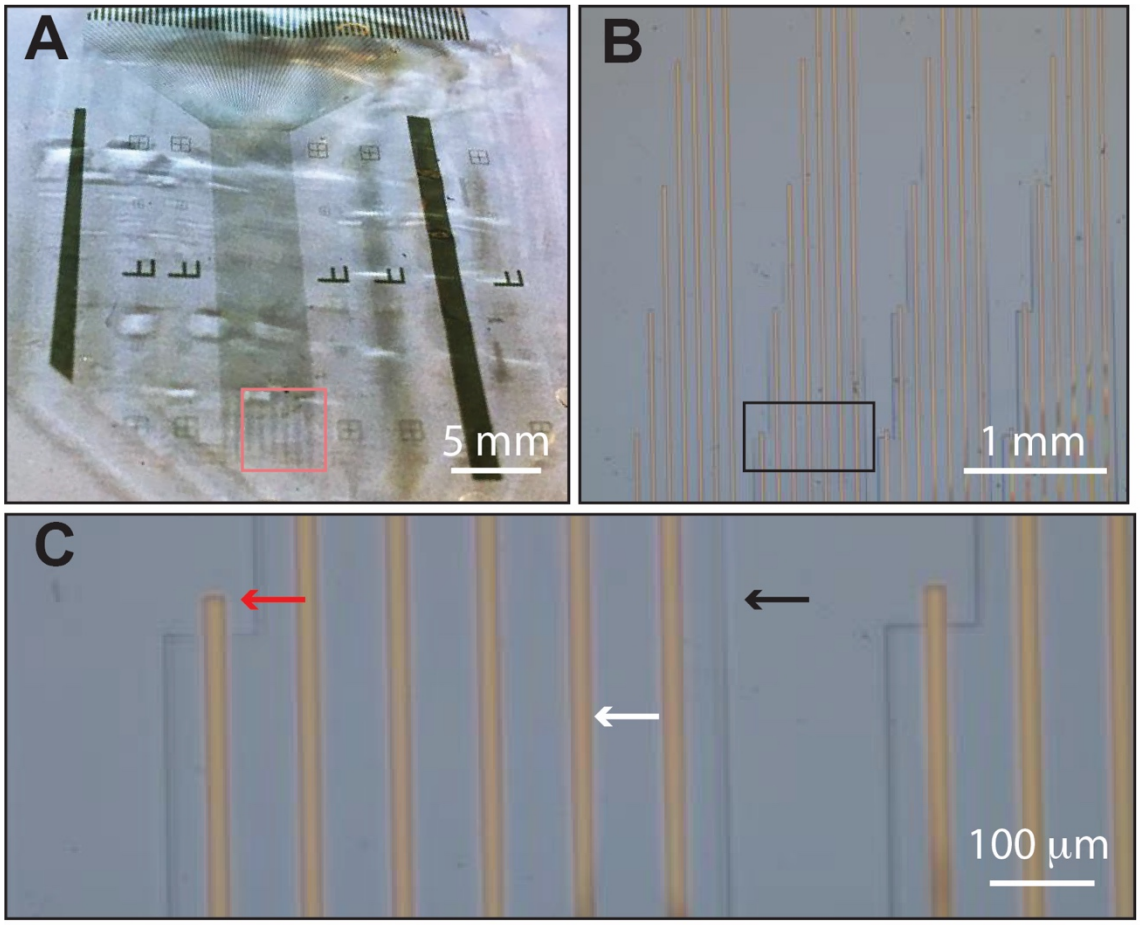

Fig. S2. Ultra-high-density elastrode array. (A) Optical photographic image shows the high-density array. (B) Optical microscope image further illustrates the patterned electrodes array in the red box highlighted in (A). (C) Zoomed-in image of the black box highlighted in (B) shows individual sensor with sensing region, interconnections and elastic passivation highlighted by red, white and black arrows, respectively.

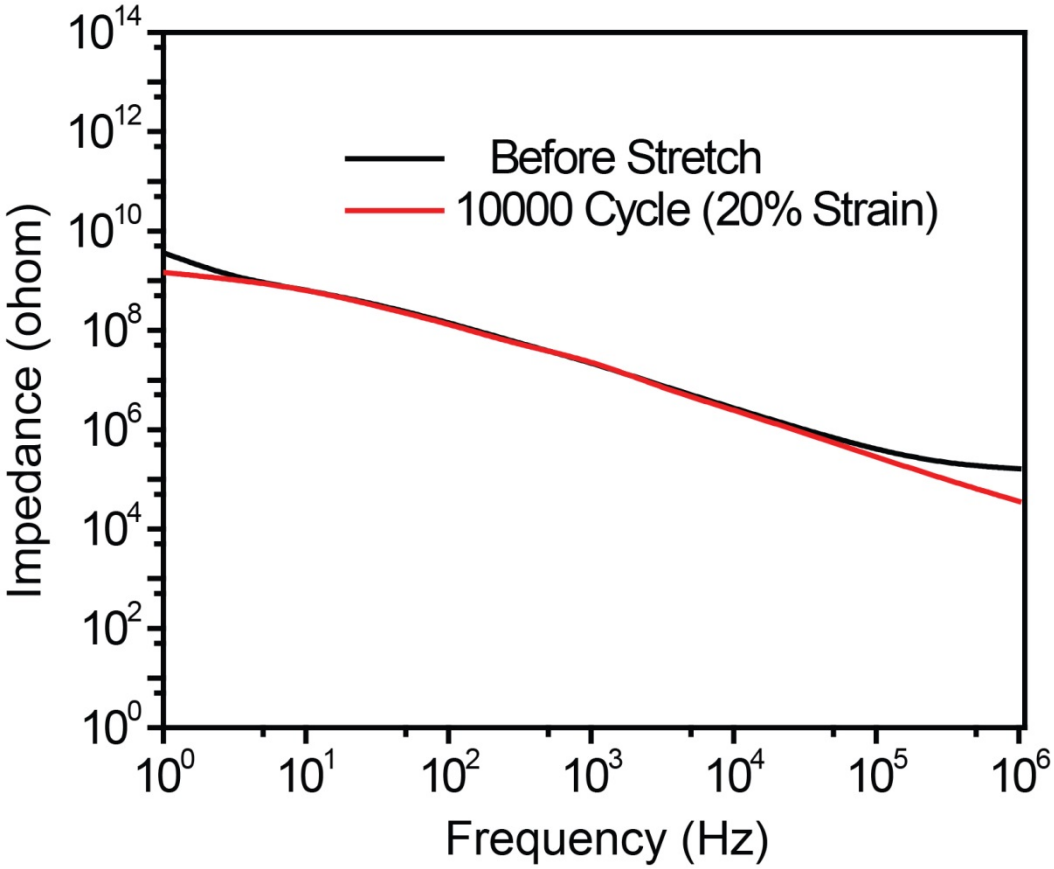

Fig. S3. Electrochemical impedance spectrum of the passivation before and after 10,000 cycles of stretching. Black and red curves show the impedance of a representative elastrode before and after 10,000 cycles with 20% strain.

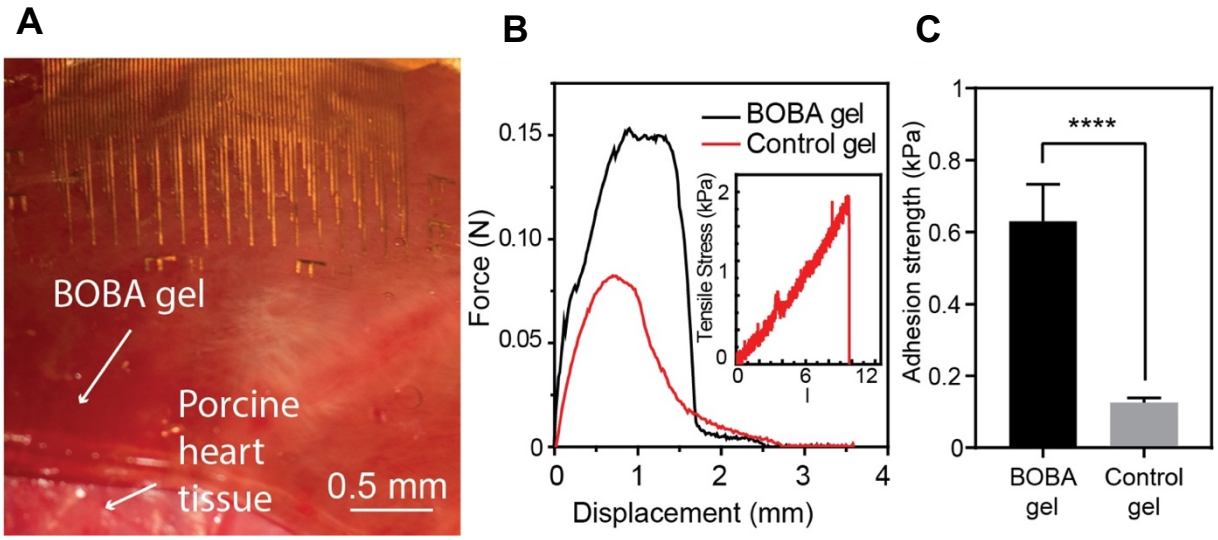

Fig. S4. Bio-organic bio-adhesive (BOBA) hydrogel for bonding elastrode array on a porcine heart. (A) Optical photographic image shows that a BOBA hydrogel bonds to the elastrode array on the right ventricular surface of a porcine heart. (B) Force-displacement curves show adhesive forces between different hydrogels and porcine heart. (C) Statistical result shows enhanced adhesion strength of the BOBA gel compared to the control hydrogel (n=3). Data are shown in mean ± s.e.m. **** represents $p < 0.0001$ from unpaired, t-test.

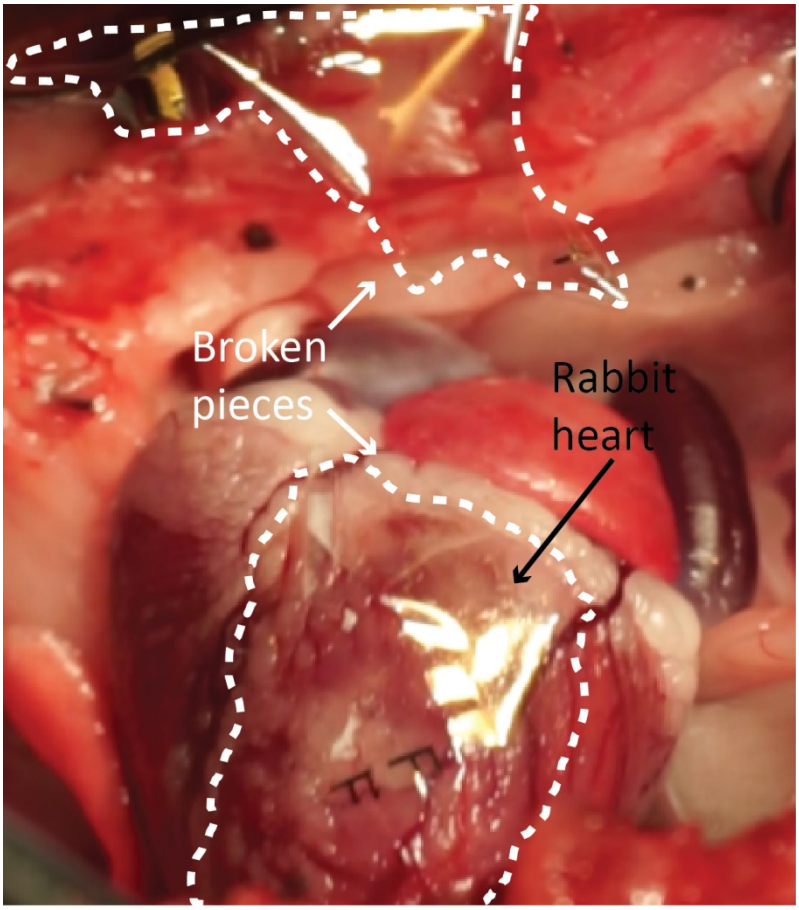

Fig. S5. Flexible ultra-thin electrodes array with the tissue-level bending stiffness attached to the surface of a beating rabbit heart *in vivo*. Flexible electrodes array made by gold electrodes and SU-8 was placed on the surface of a rabbit heart *in vivo*. Due to the displacement and contraction of the rabbit heart, the flexible electrodes array was torn apart instantly after adhered to the heart. White dashed lines highlighted the boundary of the broken device.

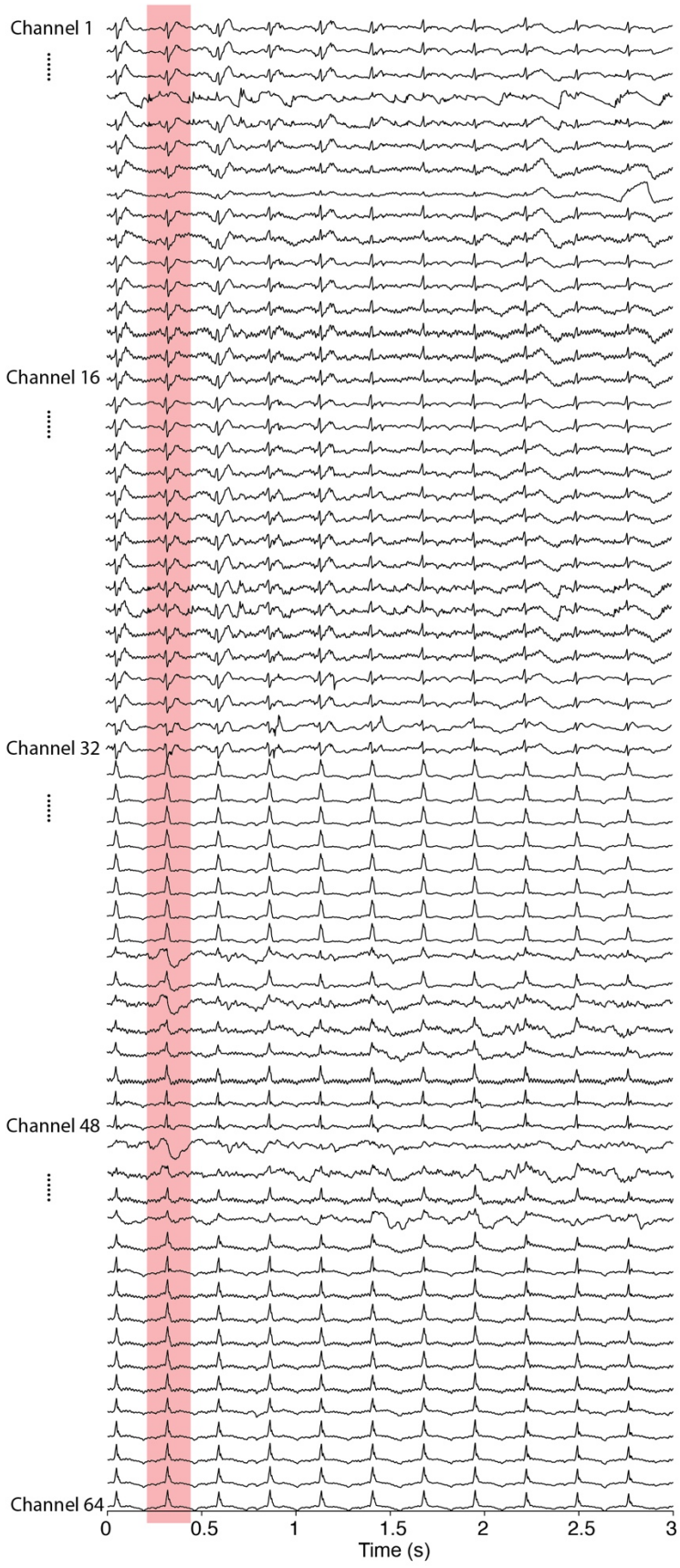
Channel 1
Channel 16
Channel 32
Channel 48
Channel 64
0
0.5
1
1.5
2
2.5
3
Time (s)

Fig. S6. Normalized voltage traces of electrogram recording from all 64 channels from the device shown in Fig. 3D. The signals are recorded from the anterior ventricular surface of a rabbit heart, with BOBA gel applied for the enhanced adhesion. The different waveforms (highlighted by the red area) of the signals between each channel show the signals recorded from different cells on the surface of the heart.

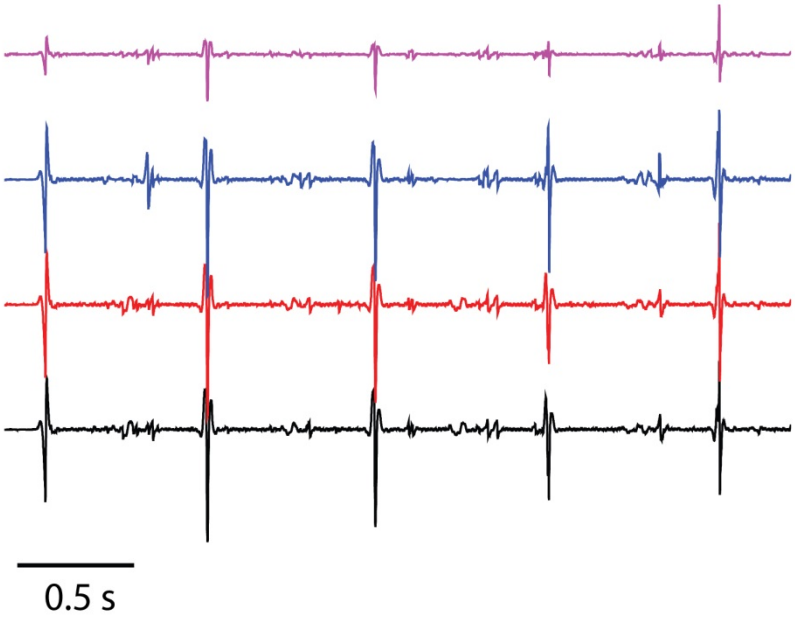

Fig. S7. Representative single voltage trace recording from the epicardial surface of ventricle in the porcine model.

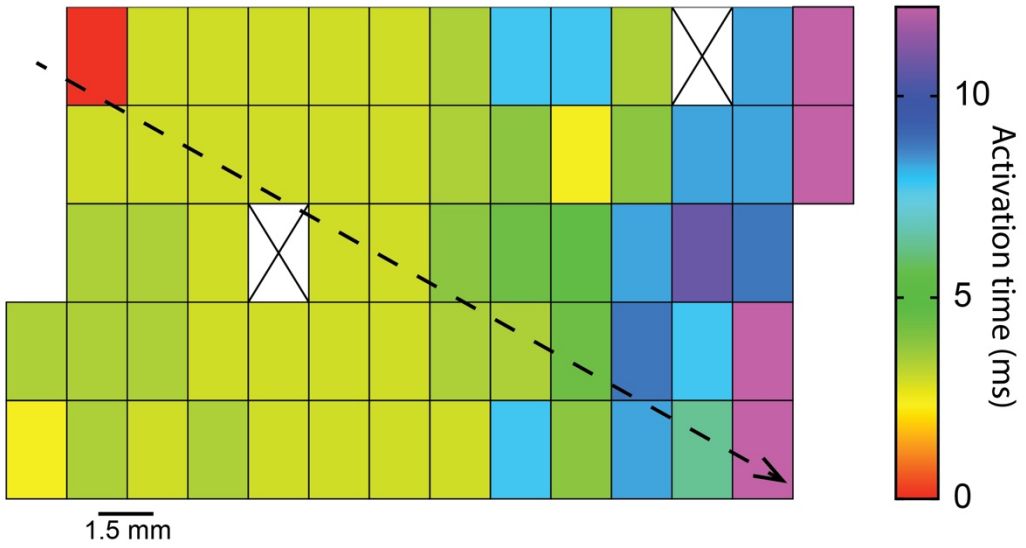

Fig. S8. Color map showing relative activation times calculated from signals captured by the elastrode array on the epicardial surface of the atria in the porcine model during normal sinus rhythm. Dotted line with arrow indicates the directionality of the signal progression. Crossed boxes are due to the failed electrodes.

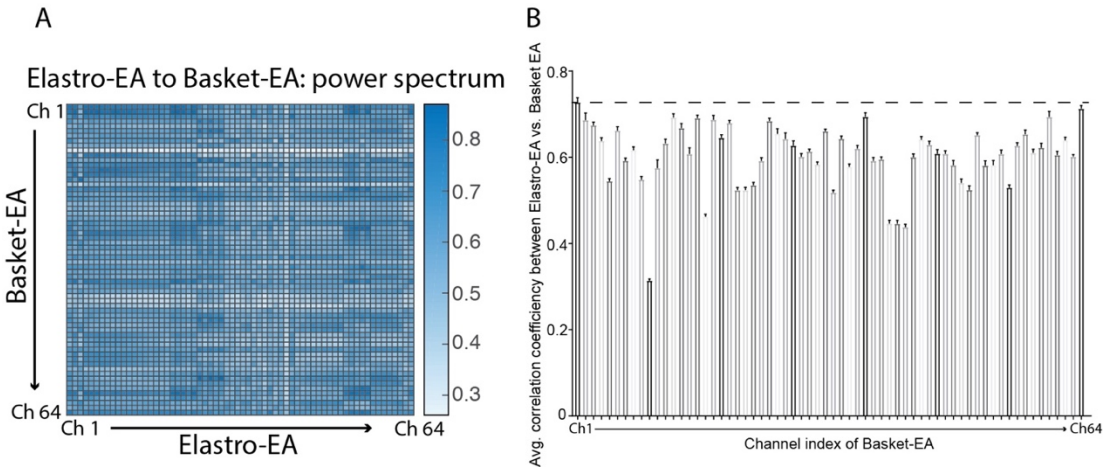

Fig. S9. Power spectrum correlation efficiency between elastrode array and basket electrode array measured on the porcine model with chronic AF shown in **Fig. 5** suggests the closed recording regions. (A) Heat plot of cross-correlation matrix of the power spectrum of epicardial signals from each elastrode to that of endocardial signals from each basket electrode. (B) Statistic summary of the averaged (64 channels) correlation efficiency between elastrode and basket electrode array. The dashed line highlights the highest correlation efficiency of 64 channels elastrodes to the Channel #1 in basket electrode array. All data are shown in mean ± s.e.m..

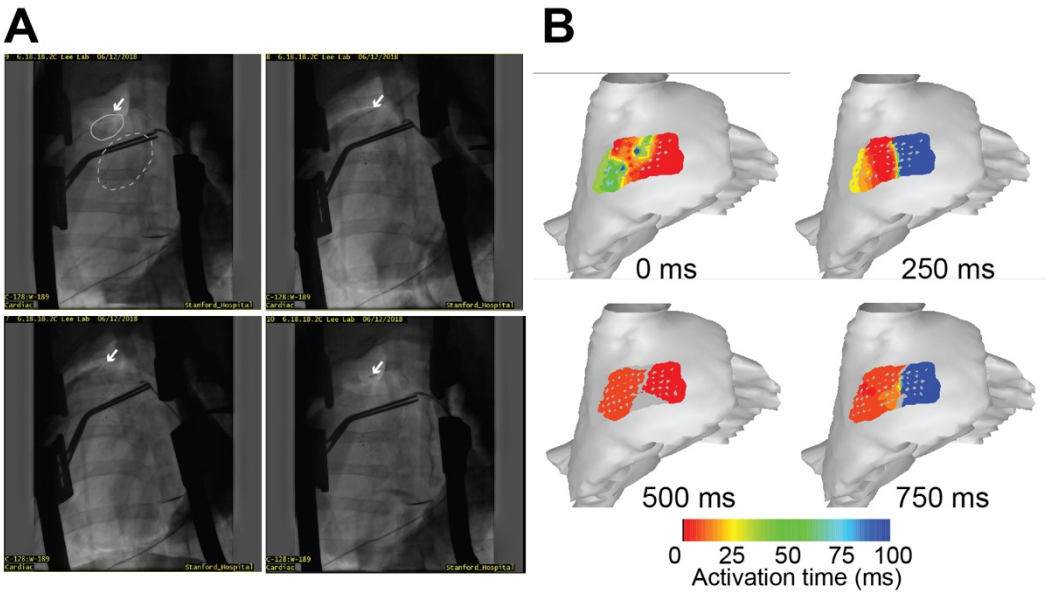

Fig. S10. Imaging of elastrode array for activation mapping correction for the porcine model. (A) Fluoroscopic images of elastrode array on the epicardial surface of the right atrium and and basket electrode array inside the right atrium. The white arrows highlight the position of the metal bar clamped on elastrode array for the imaging. Gray circle and dashed circle highlight the position of elastrode array and basket electrode array, respectively. (B) Electroanatomic projection of the recorded activation map from elastrode array for chronic AF on the surface of the porcine heart shows the relative position between elastrode electrode array and the right atrium of the heart.

Supporting Movie Legend

Movie S1. Representative elastrode array on the epicardial surface of the superior right atrium in a porcine model for electrical recording. The intrinsic stretchability and ultra-flexibility of the elastrode array effectively prevented sliding and delamination from the epicardial surface during expansion/contraction of the right atrium *in vivo*.